Eric S. Kasischke
Robert A. Shuchman
David R. Lyzenga
Radar Division
Environmental Research Institute of Michigan
Ann Arbor, MI 48107
Guy A. Meadows*
Department of Atmospheric and Oceanic Science
The University of Michigan
Ann Arbor, MI 48109

Detection of Bottom Features on Seasat Synthetic Aperture Radar Imagery

Seasat SAR imagery was evaluated with respect to its potential to assist hydrographers in identifying submerged hazards.

Abstract: *A distinct set of surface patterns detected in imagery collected by the Seasat snythetic aperture radar (SAR) have been shown to be the result of an interaction between a physical oceanic process and a bottom topographic feature. These patterns can be used to infer a bottom feature, and thus are a potential source of information for identifying submerged features hazardous to surface navigation. The Seasat SAR imaged bottom-related surface patterns in both deep and shallow water. Examples of these surface patterns are presented in this paper along with explanations of how they occur.*

Introduction

Up-to-date hydrographic information has always been of utmost importance to navigators and coastal engineers. The advent of sonar sounding techniques and the use of advanced satellite location systems has greatly aided in the generation of more current bathymetric information, but there are still shortcomings in a high percentage of nautical charts. It has been estimated that 62 percent of the world's ocean areas have insufficient hydrographic data to determine the sea-floor topography (Kapoor, 1976).

Recent political developments and economic events have led navigators to seek out and use new shipping lanes, which are not as well surveyed as traditional routes. The construction of deep draft vessels (close to thirty metres) requires a minimum water depth which is deeper than many traditional routes provide. In addition, increasing energy costs have forced many navigators to use shorter, but less well surveyed, routes.

Accurate hydrographic information is also required for coastal engineering. This need was dramatically illustrated through the extensive damage to a two-kilometre breakwater (being constructed for a deep water, bulk cargo port) at Sine, Portugal during a winter storm of moderate strength in February of 1978. A detailed wave refraction analysis after this storm revealed that the waves from this storm were refracted by the bottom and concentrated into several areas along the breakwater, causing a concentration of wave energy greater than the design specifications of the structure and resulting in extensive damage at these points. Inadequate hydrographic charts were one of the reasons cited for this design flaw (Zwamborn, 1979).

Although the demand for updated nautical

* Also a consultant at the Environmental Research Institute of Michigan.

Photogrammetric Engineering and Remote Sensing,
Vol. 49, No. 9, September 1983, pp. 1341-1353.

0099-1112/83/4909-1341$02.25/0

charts is high, the ability of the survey vessels of today's hydrographic services to fulfill these needs is deficient. For example, a recent study by the British Hydrography Study Group (Haslam, 1975) indicated that it would require 284 ship-years of work to properly survey the waters around the British Isles and another 300 ship-years to survey foreign areas for which they were responsible.

During the 1970s, the U.S. Defense Mapping Agency's Hydrographic/Topographic Center (DMAHTC) began to explore the use of remote sensing techniques to aid in the updating of nautical charts (see Hammack, 1977). The goals of using remote sensing are, in order of priority (J. C. Hammack, DMAHTC, personal communication, 1982):

- To detect uncharted or mispositioned submerged features which are potentially hazardous to surface navigation;
- To define the boundary and location of these hazardous features in either an absolute or relative sense; and
- To extract accurate, detailed, and complete water depth information.

Most remote sensing efforts in this area have utilized aerial photography, multispectral scanners, or lidars (e.g., Hammack, 1977; Lyzenga, 1981). These optical techniques have been able to meet DMAHTC's three goals in shallow-water areas which have clear water. However, these techniques break down when either the water depth or the turbidity exceed certain limits. Recently, DMAHTC has funded research to demonstrate the utility of synthetic aperture radar imagery for meeting its goals in areas where optical techniques are not applicable (Kasischke *et al.*, 1980; 1982). The purpose of this paper is to discuss the phenomena and mechanisms which are responsible for the appearance of depth-related patterns on SAR imagery, and to present examples of patterns on Seasat SAR imagery collected over oceanic regions which can be used to infer the presence of a bottom feature.

Background

The data to be presented in this paper were collected by the Seasat satellite. Among the instrumentation carried by Seasat, which was launched on June 28 1978, was an imaging synthetic aperture radar (SAR). This satellite collected over 500 passes of SAR data before suffering a catastrophic power loss in October of 1978. The SAR on board Seasat was an L-band (23.5-cm wavelength) radar. It collected 25 by 25 m resolution imagery with a ground swath-width of 100 km and a length of up to 4000 km, and viewed the surface of the Earth with an average incidence angle of 20°. For a detailed description of the Seasat SAR system and its mission, see Jordan (1980), Beal *et al.* (1981), or Fu and Holt (1982).

Even though the Seasat satellite failed just three months into its expected one-year mission, it provided over one-hundred million square kilometres of SAR imagery. These data provided the oceanography community with an unparalleled opportunity to view the surface of most of the Atlantic Ocean and portions of the Pacific Ocean within the Northern Hemisphere.

An imaging radar such as the Seasat SAR is an active device that senses the environment with short wavelength electromagnetic waves. As an active sensor, the Seasat SAR provided its own illumination in the microwave region of the electromagnetic spectrum and thus was not affected by diurnal changes in emitted or reflected radiation from the Earth's surface. Additionally, the 23.5-cm wavelength utilized by the Seasat SAR allowed for imaging the Earth's surface through clouds and light rain.

The principle in imaging any ocean surface with a radar is that the backscatter of microwave energy (echo) received by the radar contains information on the roughness characteristics (shapes, dimensions, and orientations) of the reflecting area. Parameters that influence the SAR image of the ocean surface include the motion of the scattering surfaces, coherent speckle, system resolution, and noncoherent integration as well as the surface roughness. In addition, the orientation of ocean waves and of bottom topographic features with respect to the radar "look" direction are influencing parameters.

Several scattering models exist that attempt to explain ocean surface image formation with synthetic aperture radars. These models are of two types: static models that depend on instantaneous surface features, and dynamic models that employ surface scatterer velocities.

Three static models have been suggested to describe the radar scattering of energy from large areas on the ocean surface. These three scattering models include (1) the specular point model which is most appropriate for small incidence angles, (2) the Bragg-Rice scattering model, described below, and (3) a Rayleigh scattering model which is often used in terrestrial Earth scattering calculations. There is general consensus within the radio-oceanography scientific community that a Bragg-Rice scattering theory best explains the SAR observed backscatter values obtained from the ocean surface for incidence angles between 20° and 60° (Shuchman *et al.*, 1981). The Bragg-Rice scattering model is based on a well known phenomena in the study of crystals, grating, and periodic structures. If one considers the random ocean surface to be represented by a combination (i.e., spectrum) of periodic surfaces, then the spectrum region which satisfies the backscatter phase matching condition will be the main contributor to the backscatter cross section. Sometimes in the literature, this phase matching of the small ocean

Bragg waves with the radar electromagnetic energy is termed a resonance phenomenon; more correctly stated, it should be termed a constructive interference between the electromagnetic and ocean waves.

Pioneering theoretical and experimental work by Wright (1966) at the Naval Research Laboratory (NRL) demonstrated the general validity of a Bragg scattering model for an ocean surface imaged by radar. In a series of wave tank measurements using 3-cm and 25-cm wavelength continuous wave (CW) Doppler radars, Wright demonstrated that Bragg scattering, that is, transmitted radar energy with wave number K interacts in a resonant or interference fashion with ocean surface waves with wave number K_w such that

$$K_w = 2K \sin \phi, \tag{1}$$

where $K_w = 2\pi/L$, and $K = 2\pi/\lambda$ (L and λ are the wavelengths of the surface waves and the radar, respectively), and ϕ is the incidence angle. Shuchman *et al.* (1981) showed that a Bragg scattering equation satisfactorily explained the radar backscatter return from SAR using data collected during the Marineland experiment (for a discussion of the Marineland experiment, see Shemdin (1980)). It should be noted that radar data of large ocean areas (1 by 1 km) were averaged in that analysis. Thus, based on the above, the principal radar reflectivity mechanism of imaging ocean surfaces is via the capillary and small gravity waves which produce Bragg scattering (Raney and Shuchman, 1978).

Synthetic aperture radars are also sensitive to the motion of scatterers present in the imaged scene (Raney, 1971). Effects of scatterer motion on SAR imagery may include (1) image displacement, smearing, and loss of focus in the azimuth direction; and (2) loss of focus in the range direction. Some of these effects can be removed during processing of the SAR signal histories by making appropriate adjustments to the processor (Shuchman, 1981). Effects which cannot be removed during processing may reduce the detectability of gravity waves, but are not expected to have a large influence on the depth-related image features.

Loss of focus in the range direction is due to a rotation of the phase history of the target (i.e., migration through range cells). This loss of focus is proportional to the range velocity and the integration time, and can be corrected by a rotation of the lenses in the optical processor, assuming the range velocity is constant during the integration time.

Loss of focus in the azimuth direction can be caused by the constant velocity in the azimuth direction or a changing velocity (i.e., an acceleration) in the range direction. These effects can be corrected by a change in the azimuth focus setting of the processor, assuming that the azimuth velocity and radial acceleration are constant. Because they are both inversely proportional to the platform velocity, these effects are less important for the Seasat than for aircraft SAR systems.

A variety of processes can alter the surface Bragg waves, resulting in a distinct pattern on SAR imagery. These include oceanic processes (currents, gravity waves, internal waves, slicks, local water depth variations, water temperature, and salinity), climatic processes (wind, rain, and air temperature), and man-made phenomena (ships, buoys, and oil spills). It is the hydrodynamic interaction between several of the oceanic processes and a distinct bottom feature which allows that feature to be detected on SAR imagery. Examples of these bottom-induced surface patterns will be presented in this paper. For examples of other surface patterns on Seasat SAR imagery, see Gower (1981), Beal *et al.* (1981), or Fu and Holt (1982).

Observations

This study examined over 100 passes of Seasat SAR imagery for evidence of bottom-related surface signatures. In examining Seasat SAR imagery of oceanic areas, those signatures which could be attributed to other oceanic or climatic processes (e.g., gravity waves, wind patterns, rain patterns, etc.) were eliminated from consideration. The positions of the unidentified patterns which were suspected to be bottom-induced were determined by identifying known land areas or through the use of satellite ephemeris records. Hydrographic charts from these areas were examined to determine whether or not the patterns occurred over a distinct bottom feature.

Furthermore, to determine the causes of the bottom-related surface patterns on the SAR imagery, a set of ancillary environmental data was compiled and analyzed for most test areas. These ancillary data included wind speed and direction, tide height, direction and tidal current velocity and gravity wave height, length, and dominant direction of propagation.

Finally, a third analysis was conducted which compared Seasat SAR imagery collected over the same test sites on different dates; i.e., a multitemporal analysis. This analysis was intended to determine how frequently a bottom feature appeared on the SAR imagery in a given area for a set of environmental conditions. Also, when coupled with ancillary environmental data, this technique provides a particularly powerful means for defining the limitations of detecting bottom features on SAR imagery.

Of the 100 orbits of Seasat-SAR imagery examined, approximately 50 percent was found to contain patterns on the imagery which could be correlated to a distinct bottom feature. Of these, 35 orbits were rigorously examined and the surface patterns on the imagery compared with hydrographic charts and ancillary data (environmental conditions coincident with the satellite overpass). These orbits are presented in Table 1. Also in-

TABLE 1. SUMMARY OF SEASAT SAR IMAGERY EXAMINED FOR BATHYMETRIC FEATURES

Study Site (Location)	Seasat Revolution	Date	Time (GMT)	Bottom Feature(s)*	SAR Signature(s)*
Little Bahama Bank—					
Grand Bahama Island	407	25 July 1978	12:46	EB	SB
	651	11 August 1978	12:26	EB	SB
Great Bahama Bank—Bimini	407	25 July 1978	12:46	EB	SB
	651	11 August 1978	12:26	EB	SB
Great Bahama Bank—	407	25 July 1978	12:46	EB	SB
Southern Edge	651	11 August 1978	12:26	EB	SB
Tongue of the Ocean	450	28 July 1978	06:23	EB, SWS	SB, SP
	529	02 August 1978	18:37	EB, SWS	SB, SP
	694	14 August 1978	07:37	EB, SWS	SB, SP
	1024	06 September 1978	09:18	EB, SWS	SB, SP
	1110	12 September 1978	09:43	EB, SWS	SB, SP
	1153	15 September 1978	09:56	EB, SWS	SB, SP
	1196	18 September 1978	10:09	EB, SWS	SB, SP
	1239	21 September 1978	10:21	EB, SWS	SB, SP
	1282	24 September 1978	10:34	EB, SWS	SB, SP
	1325	27 September 1978	10:47	EB, SWS	SB, SP
	1368	30 September 1978	11:00	EB, SWS	SB, SP
	1411	03 October 1978	11:12	EB, SWS	SB, SP
Haiti—Rochelois Bank	492	31 July 1978	11:28	SI	SB, SP
Bermuda	1267	23 September 1978	14:20	SI	SB
Nantucket Shoals	880	27 August 1978	12:25	SWS	SP
Cook Inlet, Alaska	289	17 July 1978	11:50	SWS, MB	SP, OB
North Rona Rock	762	19 August 1978	06:41	SI	OB
Sula Sgier	762	19 August 1978	06:41	SI	OB
English Channel	762	19 August 1978	06:41	SWS, MB	SP, DB
	957	01 September 1978	21:40	SWS	SP, DB
	1430	04 October 1978	20:42	SWS	SP
	1473	08 October 1978	00:15	SWS	SP
North East Atlantic	547	04 August 1978	06:15	DWB, DWR, DWS, DWSM	FB, IW
	556	04 August 1978	21:35	DWB, DWR, DWS, DWSM	FB, IW
	599	07 August 1978	21:43	DWB, DWR, DWS, DWSM	FB, IW
	633	10 August 1978	06:29	DWB, DWR, DWS	FB, IW
	642	10 August 1978	21:50	DWR, DWS, DWSM	FB, IW
	719	16 August 1978	06:43	DWB, DWR, DWS	FB, IW
	757	18 August 1978	22:40	DWB, DWR, DWS	FB, IW
	762	19 August 1978	06:41	DWB, DWR, DWS	FB, IW
	791	21 August 1978	07:24	DWB, DWR, DWS, DWSM	FB, IW
	834	24 August 1978	07:30	DWB, DWR, DWS	FB
	958	01 September 1978	23:54	DWB, DWR	FB, IW
	1006	05 September 1978	08:15	DWB, DWR, DWS	FB, IW
	1044	08 September 1978	00:18	DWB, DWR	FB, IW
	1049	08 September 1978	08:27	DWB, DWR, DWS	FB, IW
	1087	11 September 1978	00:30	DWB, DWR	FB, IW

*Bottom Feature Key
DWB: Deep Water Bank
DWR: Deep Water Ridge
DWS: Deep Water Shelf
DWSM: Deep Water Seamount
EB: Edge of Great or Little Bahama Bank
MB: Mud Bank
SI: Shoal area surrounding an island
SWS: Shallow Water Sand Bank

**SAR Signature Key
DB: Change in radar backscatter or tone (see Figure 2)
FB: Frontal Boundary (see Figure 6)
IW: Internal Wave (see Figure 5)
SB: Stripe along Great or Little Bahama Bank (see Figure 3)
SP: Striated pattern (see Figure 3)

cluded in Table 1 are the study site and its location, the date and time of the Seasat orbits, the type of bottom feature at that site, and the type of SAR surface pattern observed. SAR imagery from four areas which demonstrate SAR's ability to detect bottom features is presented in the following sections.

Table 2 summarizes the types of bottom-related surface patterns observed on Seasat SAR images. This table also includes the hypothesized oceanic process which interacts with a bottom feature to perturb the short surface capillary and ultra-gravity waves, which are then detected by a SAR. The two major ocean processes that result in SAR observation of submerged features are (1) gravity waves propagating into shallow water, and (2) oceanic currents flowing over distinct bottom features. These processes can result in five distinct surface patterns on SAR images, as will be discussed in the following sections.

Shallow Water Features

The first type of commonly observed bottom-related feature with a corresponding expression or surface pattern on SAR imagery is that associated with changes in wavelength and direction of ocean swell entering coastal regions. Utilizing linear gravity wave theory and applying Snell's Law, relative changes in wave phase speed can be successively calculated relative to a bathymetric grid. Hence, topographically induced changes in both surface wavelength and direction can be calculated at each grid location as a function of water depth. Because Seasat SAR imagery can be used to derive accurate estimates of wavelength and direction (see Kasischke, 1980; Gonzalez *et al.*, 1981; Vesecky *et al.*, 1982), the mathematical relationship between wavelength and direction and water depth can be used to calculate water depth. The Seasat SAR's ability to detect changes in wavelength and direction of an ocean swell propagating into shallow coastal waters was first demonstrated by Shuchman and Kasischke (1981). Figure 1 shows a plot of water depths which were calculated using estimates of wavelength obtained from Seasat SAR imagery compared to water depths from a hydrographic survey.

The second type of bottom-related surface pattern observed on Seasat SAR imagery is associated with an ocean swell propagating over a distinct topographic irregularity in the sea bottom. When a gravity wave field crosses an abrupt change in the water depth, the structure of the gravity wave is changed because the wave begins a transition from a deep water to shallow water wave. As this transformation proceeds, the mass transport and horizontal particle velocity at the surface increases, thus straining the small scale surface roughness field (i.e., the capillary and ultra-gravity waves) and producing a corresponding change in the received electromagnetic backscatter by the radar. An example of one such feature observed by the Seasat SAR is presented in Figure 2. The image in Figure 2 was collected during Revolution 762 (19 August 1978) as Seasat passed over North Rona Rock, an island located approximately 75 km off the northwest tip of Scotland. Detected on this SAR image is a distinct change in radar backscatter in the shoal region (designated by the 50-m line) surrounding North Rona Rock. The gravity wave field present on this date is also clearly evident on the SAR imagery. Surface measurements made concurrently with the Seasat overpass about 300 kilometres west of North Rona Rock indicate a swell with a dominant wavelength of 206 m, a significant wave height ($H_{1/3}$) of 4.3 m, and a direction of propagation towards 60° (True) was present in the northeast Atlantic Ocean at this time. A wind from 186° (True) with a surface velocity of 12 m/s was also present. The diffraction of the waves as they pass North Rona Rock can also be seen.

The third class of SAR-sensed surface pattern is

Table 2. Summary of Types of Bottom-Related Surface Patterns on Seasat SAR Imagery

Bottom/Ocean Interaction	Result on Ocean Surface	Result on SAR Image
1. Gravity Wave Propagating into Shallow Water	1. Refraction of Gravity Waves	Detection of change in gravity wavelength and direction of propagation
	2. Non-linear Gravity wave interaction	Distinct change in radar backscatter resulting in change in image tone over bottom feature (see Figure 2)
2. Current Flowing over a bottom feature	1. Change in Current velocity	Distinct change in radar backscatter resulting in a banded pattern over the bottom feature (see Figure 3)
	2. Upwelling	Frontal Boundary (see Figure 6)
	3. Generation of Internal Waves	Internal Wave Pattern (see Figure 5)

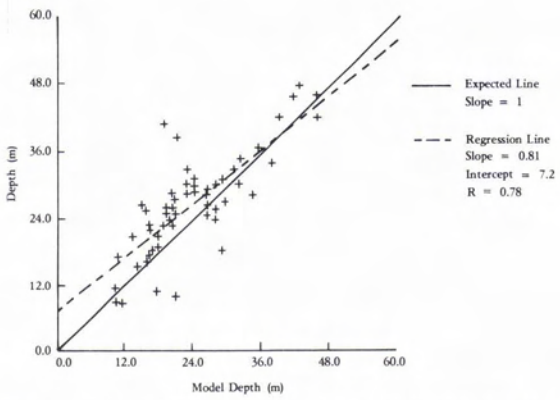

FIG. 1. Plot of water depths calculated using inverted airy wave theory with changes of wavelength extracted from Seasat SAR imagery versus depths obtained from U.S. National Ocean Surveys.

associated with a strong current flowing over a bottom feature in shallow (<50 m) water. These are perhaps the most common and readily identifiable bottom-induced patterns on SAR imagery, and several examples are presented in Figure 3. Because its velocity and internal structure are regulated by the bottom topography, a tidal current will alter the amplitude of the ocean surface Bragg wave to which the SAR is sensitive. The current's modulation of the ocean Bragg wave amplitude enables successful SAR imaging of many bottom features in shallow water.

Several researchers have previously reported surface signatures on radar imagery which are the

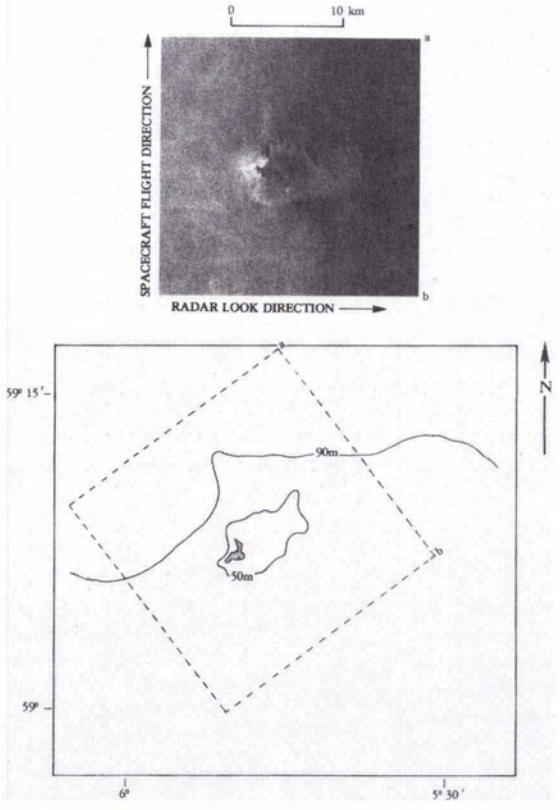

FIG. 2. Seasat SAR imagery and hydrographic chart of North Rona Rock (collected during Revolution 762, 19 August 1978) illustrating change in image tone (radar backscatter) associated with the shoal region around the island. (Seasat SAR data collected by the European Space Agency and optically processed at ERIM. Chart reproduced from DMA Chart No. 35200.)

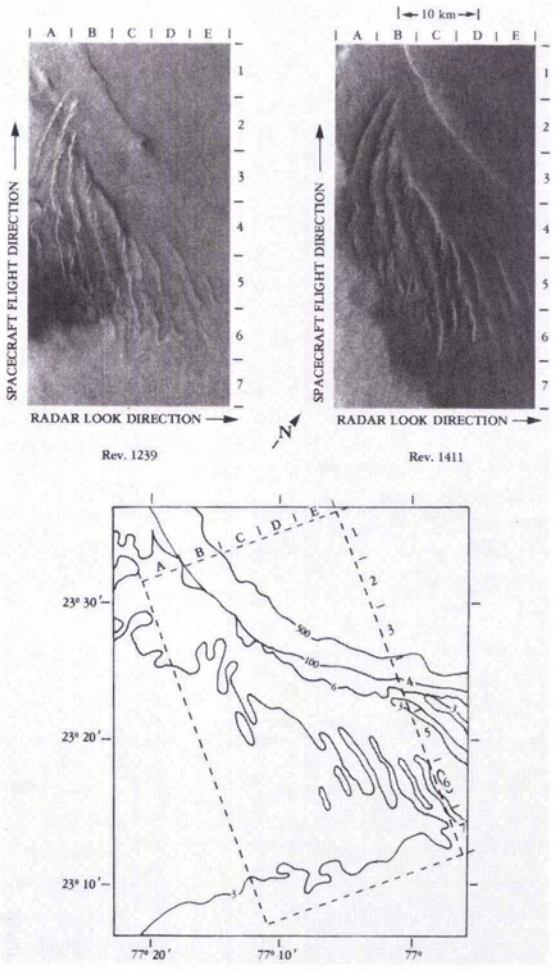

FIG. 3. Seasat SAR imagery and hydrographic chart of the Tongue of the Ocean: (1) Seasat Revolution 1239 (21 September 1978), (b) Seasat Revolution 1411 (8 October 1978), and (c) hydrographic chart of area. (Seasat digitally processed imagery courtesy of the Jet Propulsion Laboratory. Chart reproduced from DMA Chart Nos. 26300 and 27040, depths in fathoms).

result of a current flowing over the bottom feature. DeLoor and Brunsveld Van Hulten (1978) first described this phenomenon using real aperture radar imagery collected over the North Sea. Using Seasat SAR imagery, Kasischke *et al.* (1980) and Kenyon (1981) have reported detecting sand waves in the southeast corner of the North Sea. McLeish *et al.* (1981) reported sand waves detected on real aperture, side-looking airborne radar (SLAR) imagery collected off the Dutch coast. Finally, Kasischke *et al.* (1980) reported detecting sand waves and ridges in the Nantucket Shoals off the Massachusetts coast. The appearance of these current-induced shallow-water signatures is dependent on several factors, including the strength and direction of the tidal current, the shape, orientation, and depth of the bottom feature, and the magnitude of the surface wind. Shuchman (1982) determined the effects of several of these factors through an extensive hydrodynamic and electromagnetic modeling effort. The conditions required to observe these conditions include (1) a tidal current of at least 0.4 m/s (0.8 knots), and (2) a wind of at least 1 m/s (2 knots) but not greater than 7.5 m/s (15 knots), with at least some component in a direction parallel to the radar line-of-sight.

Figure 3 presents two examples of Seasat SAR images collected at the edge of the Great Bahama Bank, over a series of tidal bar belts in the southern end of the Tongue of the Ocean. The two images presented in Figure 3 were collected during Revolution 1411 (3 October 1978) and Revolution 1239 (21 September 1978). Comparison of the SAR images with the corresponding hydrographic chart (in Figure 3) reveals that the pattern located from B1 to E4 corresponds to the edge of the Great Bahama Bank, while the larger features (A2 to E5) correspond to the tidal bar belts in this area.

It should be noted that the patterns located over the tidal bar belts are "banded" in appearance, the pattern consisting of one band darker than the adjacent background image and one band lighter than the adjacent background image, and the patterns are reversed in the two images shown in Figure 3. Both of the images shown in Figure 3 were produced from Seasat SAR data which were digitally processed at the Jet Propulsion Laboratory. The differences in the patterns present over the tidal bar belts are not due to differences in the manner in which the images were processed, but are the result of different environmental conditions at the times the two data sets were collected.

The Tongue of the Ocean (TOTO) is a large (30 km by 120 km) steep-walled channel within the Great Bahama Banks. It has a depth of well over 1300 metres, while the surrounding Great Bahama Bank is generally less than ten metres deep. The tidal bar belts at the southern edge of the TOTO are a series of shallow sand banks (one to two metres deep) with five to seven metre deep channels between them.

It is postulated that the patterns present on the Seasat imagery in Figure 3 were the result of an interaction between a tidal current flowing over the distinct bottom features in this area. Although the tidal range between high and low water is only about one metre in the Bahamas, tidal currents in the tidal bar belts region of the TOTO have been reported to be between 1 and 1.5 m/s (2 to 3 knots). During a study of tidal bar belts near Schooner Cay in the Bahamas, Ball (1967) noted the tide in this area was of the standing wave variety. Using tide gage and current meter recordings, he observed that maximum current over the tidal bar belts occurred midway between high and low water, with maximum velocities between 1 and 1.5 m/s (2 to 3 knots). In a study of the tidal bar belts of the TOTO, Palmer (1979) also noted that the maximum tidal currents in this region (estimated to be in excess of 1.5 m/s) occurred midway between high and low water.

The strong tidal-driven flow of water over the tidal bar belts and off the edge of Great Bahama Bank into the TOTO may sufficiently disturb the small scale surface roughness structure (i.e., the capillary and ultra-gravity waves) to cause a corresponding change in radar backscatter. It should be further noted that, although the surface patterns occur in the same locations in the two Seasat images in Figure 3, their appearance is different. These differences can be explained through the use of the hydrodynamic/electromagnetic model developed by Shuchman (1982), a qualitative synopsis of which is given in the following paragraphs.

Examination of tide tables for the Bahamas (Kline, 1978) indicates at the time of Revolution 1411 that the tide stage was four hours before low tide, indicating the presence of an ebb flow of water off the Great Bahama Bank into the TOTO. During Revolution 1239, the tide stage was one hour before high water, indicating the presence of a flood tide onto the Great Bahama Bank from the TOTO. Weather records from the Bahama Meteorological Office at Nassau showed a north wind with a velocity of 2.5 m/s was present during Revolution 1411 while an east wind of 4.8 m/s was present during Revolution 1239.

There are three environmental factors influencing the ocean surface roughness sensed by the SAR over sand banks such as those located at the Tongue of the Ocean. These factors are the current speed, the depth of water, and the wind speed and direction. In regions where the depth (and therefore the current speed) is changing rapidly, the roughness is influenced primarily by the rate of change of the current speed. A changing current tends to increase or decrease the amplitude of the

small capillary and ultra-gravity waves on the surface and make the surface rougher or smoother, depending on the direction of the current relative to the waves.

In areas where the depth is decreasing in the direction of the current, the surface velocity of the water will increase, resulting in a decrease in the amplitude of the surface capillary waves. In areas where the depth is increasing, the surface velocity will decrease, resulting in an increase in the amplitude of the surface capillary waves. This alternating increase and decrease of the water velocity results in the banded patterns imaged by the Seasat SAR over the sand banks.

In areas where the depth and the current are nearly constant, the surface roughness is governed primarily by the wind. The wind can be thought of as a restoring force which tends to bring the wave height or surface roughness into an equilibrium value which depends on the wind speed. Thus, if current variations cause the wave height to be decreased, the wind, given sufficient time, will return the wave height to its original value. These general statements are applied to the two particular cases illustrated in Figure 3 in the following paragraphs.

It should be noted that, although the following discussion is qualitative in nature, the observations made are based on a quantitative hydrodynamic/electromagnetic model developed and tested by Shuchman (1982). Computer simulated SAR imagery generated using this model of a tidal driven current flowing over sand banks in the English Channel and the Nantucket Shoals (almost identical to the situation occurring at the Tongue of the Ocean tidal bar belts) compared favorably to actual Seasat SAR images collected over these regions.

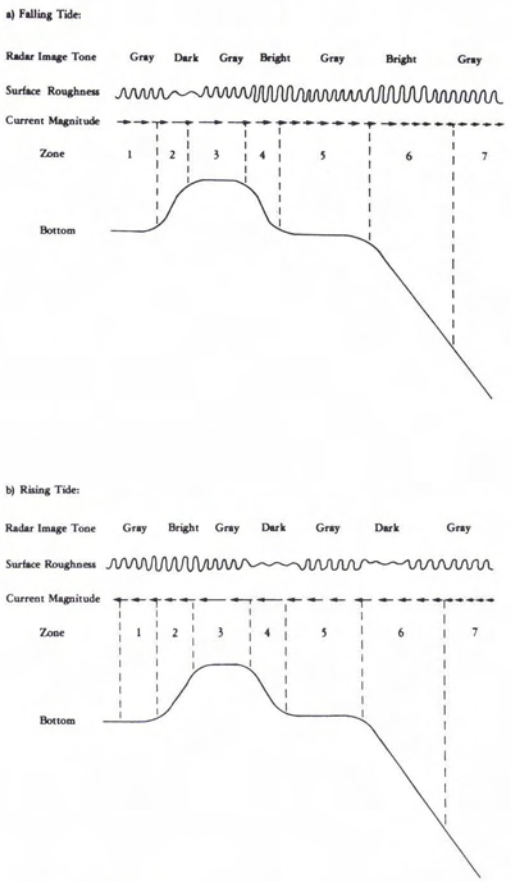

FIG. 4. Schematic diagram of interactions of current, bottom, and capillary waves and the resultant SAR image intensity variation.

The bottom topography for the southern edge of the TOTO may be modeled and divided into seven regions as illustrated in Figure 4. The pattern of surface roughness variations depends on the current direction. For simplicity, in both of these cases the waves are assumed to be propagating in the same direction as the current. Essentially the same qualitative descriptions hold if the waves are propagating in the opposite direction to the current except that the phenomenon of wave blockage can occur if the current velocity changes from less than the group velocity of the waves to larger than this velocity. For a falling tide (Figure 4a) the following interactions occur:

Region 1: The depth is assumed to be uniform over a large enough area so that the wave height (surface roughness) has reached an equilibrium value for the existing wind speed and current conditions.

Region 2: Decreasing depth causes an increasing water current which in turn causes a progressive smoothing out of the surface roughness pattern (i.e., a decrease in the amplitude of the capillary and ultra gravity waves).

Region 3: The current remains constant while the wave height (surface roughness) is brought back into equilibrium by the action of the wind.

Region 4: Increasing depth causes a decreasing current, thus a compression of the surface, and a progressive roughening of the surface.

Region 5: Depth and current remain constant while the wave height readjusts into equilibrium with the wind.

Region 6: Similar to region 4, i.e., a decreasing current causes an increasing surface roughness.

Region 7: Similar to region 5, i.e., a gradual return to equilibrium with the given wind conditions.

The above model appears to adequately describe the patterns in Figure 3 for Revolution 1411, when an ebb tidal flow was present. Note in the SAR image collected over the southern portion of the TOTO that there exists a series of ridges, each of which has a banded appearance as described in regions 1 through 5 above.

For a rising (flood) tide (i.e., a current flowing onto the bank), the following interactions occur, as illustrated in Figure 4b:

Region 7: The depth is assumed to be uniform over a large enough area so that the wave heights (i.e., surface roughness) have reached an equilibrium with the existing wind speed and current conditions, resulting in an area of uniform radar backscatter.

Region 6: A decreasing water depth causes an increasing current which in turn causes a smoothing out (damping) of the surface capillary and ultra-gravity waves.

Region 5: Gradual return to equilibrium.

Region 4: Same as Region 6.

Region 3: Gradual return to equilibrium.

Region 2: An increasing water depth causes a decreasing current which in turn causes a compression of the surface waves and a progressive roughening of the surface with respect to the incident radar waves.

Region 1: Gradual return to equilibrium.

This model appears to adequately describe the patterns present on Revolution 1239 during a flood tide.

Thus, the surface patterns present on the two Seasat SAR images in Figure 3 are consistent with the hydrodynamic/electromagnetic model developed by Shuchman (1982) and illustrated in Figure 4. All Seasat SAR images collected over TOTO during ebb flows had patterns similar to those on Revolution 1411 imagery, while all those collected during flood conditions were similar to Revolution 1239 imagery.

Deep Water Features

Several types of surface patterns observed on Seasat SAR imagery are believed to be the result of an interaction between a tidal driven current and bottom features in deep water regions such as seamounts, submarine ridges, banks, and edges of continental shelfs. These surface patterns are of two types: internal wave signatures and frontal boundary signatures. Figures 5 and 6 show Seasat SAR imagery collected over the same general region of the northeast Atlantic Ocean, which illustrate the two types of deep water patterns, while Figure 7 illustrates the bathymetry of this area.

Figure 5 presents examples of internal wave signatures. This imagery was collected during Revolution 599 on 7 August 1978 at approximately 2143 (GMT). It can be observed on this SAR image that the internal wave patterns occur over the Wyville-Thomson Ridge, which rises to within approximately 400 metres of the water surface from a surrounding deep water area of over 1000 metres in depth.

Figure 6 presents an example of a frontal boundary observed on Seasat SAR imagery collected during Revolution 762 on 19 August 1978 at approximately 0640 GMT. The curved dark line beginning at A4 and continuing to B9 is believed to

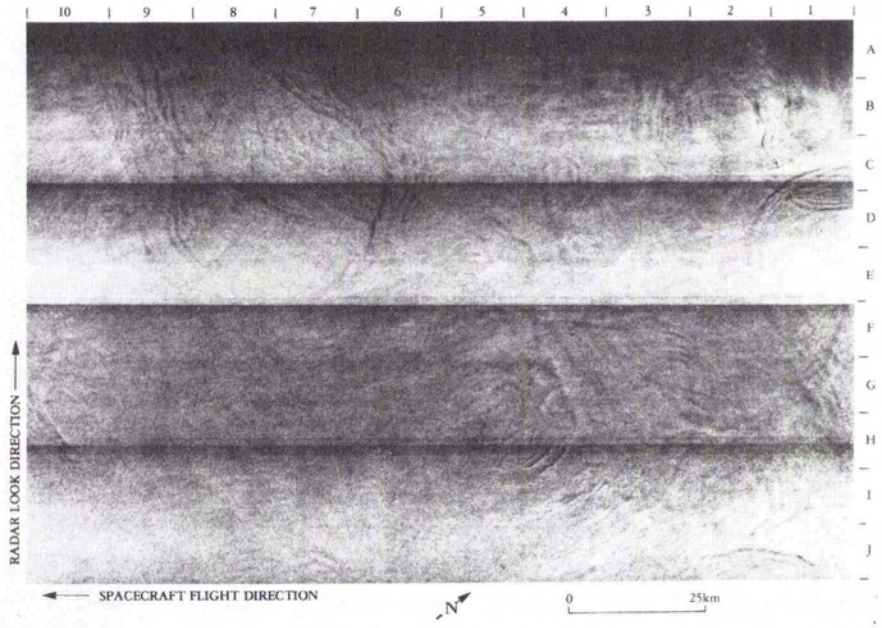

FIG. 5. Seasat SAR imagery of internal waves collected over the Wyville-Thomson Ridge (Revolution 599, 7 August 1978. Optically processed image courtesy of JPL).

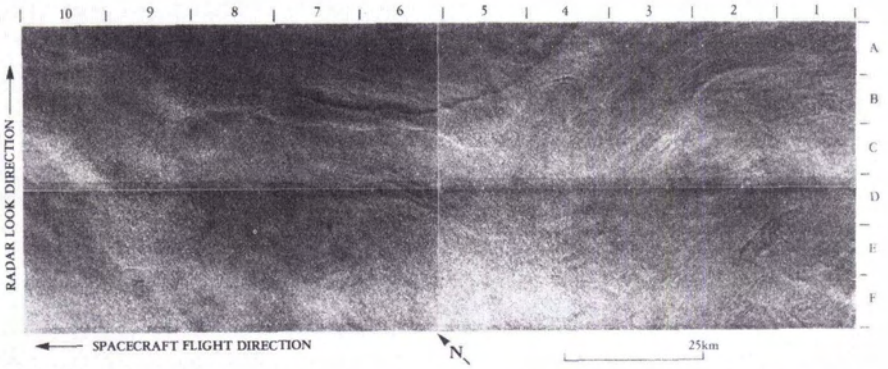

FIG. 6. Seasat SAR imagery of a frontal boundary collected over the Faeroe Bank Channel and Faeroe Ridge (Revolution 762, 19 August 1978. Optically processed image courtesy of JPL).

be a surface pattern caused by a frontal boundary. Its location appears to be in an area where the bottom is rising from the Faeroe Bank Channel to the Faeroe Shelf, over an area with a water depth between 600 and 1000 metres.

It is believed that both of these deep water signatures are the result of an interaction between a tidal current and a deep water bottom topographic feature. A current flowing over a deep water bottom feature can cause both internal waves and areas of upwelling, which result in frontal boundaries.

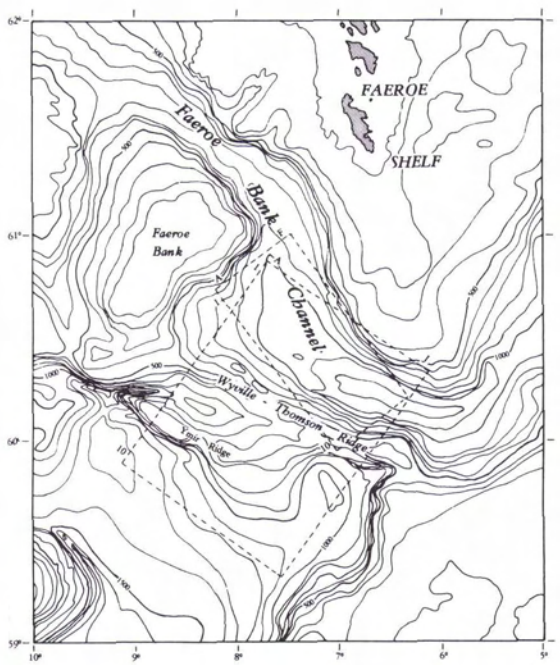

FIG. 7. Hydrographic chart of Northeast Atlantic Ocean showing locations of Figures 5 and 6 (After Institute of Oceanic Science (U.K.) Chart No. C6567, depths in metres).

There is little doubt that internal wave signatures have been observed on both aircraft and spaceborne SAR imagery collected over coastal areas (Brown *et al.*, 1976; Shuchman and Kasischke, 1979; Gower and Hughes, 1979; Apel, 1981; Fu and Holt, 1982; Vesecky and Stewart, 1982). These patterns are visible because the energy field associated with the internal wave is sufficient to alter the small scale surface roughness to which the SAR is sensitive. Based on the results of this study and other recent research (Shuchman and Kasischke, 1979; Fu and Holt, 1982), it now appears that internal wave patterns can also be detected in deep water regions.

The generation mechanisms and sources responsible for internal waves have been extensively researched during recent years (Wunch, 1976; Muller and Olbers, 1975; Bell, 1975; Baines, 1979). Even so, the knowledge of the physical processes for internal wave generation is still very limited because a determination of the sources and sinks of internal waves requires a continuous record of the wave spectra (Garrett and Munk, 1975 and 1979).

Several sources for the generation of internal waves have been identified, including surface atmospheric effects, internal (oceanic) effects, and topographic effects (Thorpe, 1975). Surface atmospheric effects include traveling atmospheric pressure and stress, buoyancy flux, surface wave interactions, and Ekman layer instability. Internal (oceanic) generation can be caused by decay of large scale circulations and breaking baroclinic instability (of which there is very little known). The generation of internal waves due to topographic features is similar to the generation of the Lee waves by air flow over irregular surfaces. In the ocean, internal waves can be generated when a current (tidal or otherwise) flows over a deep

water feature such as a seamount, guyot, submarine ridge, or the edge of a continental shelf (Wunch, 1975; Bell, 1975; Baines, 1973).

It is suspected that tidal currents flowing over the bottom topographic features in the northeast Atlantic were forming internal waves along the thermocline present in this area. In many cases, the internal wave fields are felt to have sufficient energy to modulate the surface capillary wave structure, and hence allow the internal waves to be detected on SAR imagery, as illustrated in Figure 5.

The image presented in Figure 5 is not an isolated example of an internal wave pattern in a deep water region. Seasat imagery collected during the Joint Air/Sea Interaction over the northeast Atlantic (see Allan and Guymer, 1980) was examined during the present study. Within the total area covered by the 15 Seasat revolutions, 17 distinct bottom features existed. The bottom features in this area had depths ranging from less than 100 metres (Bill Bailey's Bank) to approximately 1000 metres (Hebrides Terrace Seamount). Seasat imaged the water surface over these features a total of 89 times. On 63 percent of these occasions, an internal wave pattern occurred. No internal wave patterns were present on the Seasat SAR imagery collected over the deep water basins (>2000 m) in the northeast Altantic.

Data presented by Bainbridge (1978) suggest that severe deformation of the thermocline can also occur as the result of a current flowing over a deep water bottom feature. This deformation is sometimes so severe as to force the colder, less saline, deeper water to the surface, resulting in an area of upwelling. This deep water upwelling would result in a frontal boundary between the two water masses. It has been shown that Seasat can detect frontal boundaries (Shuchman *et al.*, 1979; Hayes, 1981; Cheney, 1981; Lichy *et al.*, 1981), and it is believed that patterns like those in Figure 6 are patterns caused by frontal boundaries. On 38 percent of the occasions that Seasat imaged the water surface over a deep water bottom feature in the northeast Altantic, a pattern identified as a frontal boundary was present.

Summary and Conclusions

This study has shown that certain patterns on SAR imagery can be used to infer the presence of a bottom topographic feature located in the vicinity of the pattern. These SAR observed patterns can occur in both shallow coastal regions as well as in deeper offshore water. It has been demonstrated that SAR imagery can be used to detect submerged bottom features which are potentially hazardous to surface navigation.

The frequency with which bottom-induced surface patterns appear on spaceborne SAR imagery must also be determined in order to define the utility of this data source for providing information in updating nautical charts. Analysis of Seasat imagery collected over the English Channel showed that the larger sand banks were detected 75 percent of the time while the smaller sand banks were detected only 50 percent of the time. Analysis of the Seasat imagery collected over the Tongue of the Ocean showed that distinct surface patterns occurred more than 90 percent of the time over the tidal bar belts and 70 percent of the time over the edge of the Great Bahama Bank. Finally, in the deep water study, an internal wave pattern was present on 63 percent of the Seasat imagery collected over deep water features such as a seamounts, ridges, or banks.

Currently, all SAR imagery collected by the Seasat SAR and the Shuttle Imaging Radar (SIR-A) is being examined and the number of times a surface pattern occurs, or does not occur, over a bottom feature is being tabulated.

Many spaceborne SAR systems will be deployed during the next decade. These SARs include Radarsat (Canada), Earth Resources Satellite-1 (ESA), Earth Resources Satellite-1 (Japan), SIR-B (USA), and the Microwave Remote Sensing Experiment (West Germany), to name a few. It is therefore highly likely that SAR imagery will be collected over areas where insufficient hydrographic information exists. This SAR imagery will certainly represent a data source for identifying and locating uncharted or altered bottom features for those organizations with the responsibility in updating nautical charts.

Acknowledgments

The work reported here was supported by the Defense Mapping Agency (DMA) under Contract No. 800-78-C-0060 and by the Naval Research Laboratory (NRL) under Contract No. N00014-B1-C-2254. The technical monitors were James C. Hammack (DMA) and Peter A. Mitchell (NRL). The authors would like to thank the following individuals at ERIM who provided assistance during various phases of the study: B. Termaat, J. D. Lyden, A. Klooster, and Y. S. Tseng. The authors would also like to thank The Jet Propulsion Lab and in particular B. Holt for providing some of the Seasat imagery presented in this report.

References

Allan, T. D., and T. H. Guymer, 1980. Seasat and JASIN, *Int. J. Remote Sensing, 1*, pp. 261–267.

Apel, J. R., 1981. Non-Linear Features of Internal Waves as Derived from the Seasat Imaging Radar, in *Oceanography from Space*, ed. by J. F. R. Gower, Plenum Press, New York, pp. 525–533.

Bainbridge, A. E., 1980. *Geosecs Atlantic Expedition—Volume 2: Sections and Profiles*, U.S. Government Printing Office, Washington, D.C., 198 p.

Baines, P. G., 1979. Observations of Stratified Flow Over Two-Dimensional Obstacles in Fluid of Finite Depth, *Tellus, 31*, pp. 351–371.

Ball, M. M., 1967. Carbonate Sand Bodies of Florida and the Bahamas, *Journal of Sedimentary Petrology*, 37, pp. 556–591.

Beal, R. C., P. S. DeLeonibus, and I. Katz (eds.), 1981. *Spaceborne Synthetic Aperture Radar for Oceanography*, Johns Hopkins Univ. Press, Baltimore, MD, 215 p.

Bell, T. H., Jr., 1975. Topographically Generated Internal Waves in the Open Ocean, *J. Geophys. Res., 80*, pp. 320–327.

Brown, W. E., Jr., C. E. Elachi and T. W. Thompson, 1976. Radar Imaging of Ocean Surface Patterns, *J. Geophys. Res., 81*, pp. 2657–2667.

Cheney, R. E., 1981. A Search for Cold Water Rings with Seasat, in *Spaceborne Synthetic Aperture Radar for Oceanography*, ed. by R. C. Beal, P. S. DeLeonibus, and I. Katz, Johns Hopkins Univ. Press, Baltimore, MD, pp. 161–170.

DeLoor, G. P. and H. W. Brunsveld Van Hulten, 1978. Microwave Measurements Over the North Sea, *Boundary-Layer Meteorol., 13*, pp. 119–131.

Fu, L., and B. Holt, 1982. *Seasat Views Oceans and Sea Ice with Synthetic Aperture Radar*, JPL Publication No. 81-120, 200 p.

Garrett, C., and W. Munk, 1975. Space-Time Scales of Internal Waves: A Progress Report, *J. Geophys. Res., 80*, pp. 291–297.

———, 1979. Internal Waves in the Ocean, *Ann. Rev. Fluid Mech., 11*, pp. 339–369.

Gonzalez, F. I., R. A. Shuchman, D. B. Ross, C. L. Rufenach, and J. F. R. Gower, 1981. Synthetic Aperture Radar Wave Observations During GOASEX, *Oceanography from Space*, ed. by J. F. R. Gower, Plenum Press, New York, pp. 459–467.

Gower, J. F. R., 1981. *Oceanography from Space*, Plenum Press, New York, NY, 997 p.

Gower, J. F. R., and B. A. Hughes, 1979. Radar and ship Observations of Coastal Sea Surface Roughness Patterns in the Gulf of Georgia, *Proc. Thirteenth Int. Symp. Remote Sens. Environ.*, Ann Arbor, MI, pp. 103–115.

Hammack, J. C., 1977. Landsat Goes to Sea, *Photogrammetric Engineering and Remote Sensing, 43*, pp. 683–391.

Haslam, D. W., 1975. *Report by the Hydrographer of the Navy*, N.P. 130, Tauton, England.

Hayes, R. M., 1981. SAR Detection of the Gulf Stream, in *Spaceborne Synthetic Aperture Radar for Oceanography*, ed. by R. C. Beal, P. S. DeLeonibus, and I. Katz, Johns Hopkins Univ. Press, Baltimore, MD, pp. 146–160.

Jordan, R. L., 1980. The Seasat-A Synthetic Aperture Radar System, *IEEE J. Oceanic Eng., OE-5*, pp. 154–164.

Kapoor, D. C., 1976. International Cooperation in Hydrography, *International Hydrographic Review*, Vol. LIII(2), Monaco.

Kasischke, E. S., 1980. *Extraction of Gravity Wave Information from Synthetic Aperture Radar Data*, Univ. of Mich. M.S. Thesis, 108 p.

Kasischke, E. S., R. A. Shuchman, and J. D. Lyden, 1980. *Detection of Bathymetric Features Using SEASAT Synthetic Aperture Radar—A Feasibility Study*, ERIM Final Report No. 135900-2-F_2, 77 p.

Kasischke, E. S., D. R. Lyzenga, R. A. Shuchman, Y. S. Tseng, B. S. Termaat, B. A. Burns, and G. A. Meadows, 1982. *The Use of Synthetic Aperture Radar to Detect and Chart Submerged Navigation Hazards*, ERIM Final Report No. 15520-1-F, Ann Arbor, MI, 221 p.

Kenyon, N. H., 1981. Bedforms of Shelf Seas Viewed with SEASAT Synthetic Aperture Radar, in *Advances in Hydrographic Surveying*, ed. M. J. Wright, Society for Underwater Technology, London, pp. 67–73.

Kline, H., 1978. *Cruising Guide to the Bahamas*, Miami, Florida.

Lichy, D. E., M. G. Mattie, and L. J. Mancini, 1981. Tracking of a Warm Water Ring Using Synthetic Aperture Radar, in *Spaceborne Synthetic Aperture Radar Imagery for Oceanography*, ed. by R. C. Beal, P. S. DeLeonibus, and I. Katz, Johns Hopkins Univ. Press, Baltimore, MD, pp. 171–182.

Lyzenga, D. R., 1981. Remote Bathymetry Using Active and Passive Techniques, *1981 International Geoscience and Remote Sensing Symposium Digest*, Washington, D.C., pp. 777–786.

McLeish, W., D. J. P. Swift, R. B. Long, D. Ross, and G. Merrill, 1981. Ocean Surface Patterns Above Seafloor Bedforms as Recorded by Radar, Southern Bight of North Sea, *Mar. Geol., 43*, pp. M1–M8.

Muller, P., and D. J. Olbers, 1975. On the Dynamics of Internal Waves in the Deep Ocean, *J. Geophys. Res., 80*, pp. 3848–3860.

Palmer, M. S., 1979. *Holocene Facies Geometry of the Leeward Bank Margin, Tongue of the Ocean, Bahamas*, University of Miami, Master's Thesis, Coral Gables, Florida.

Raney, R. K., 1971. Synthetic Aperture Imaging Radar and Moving Targets, *IEEE Trans. Aerospace Elect. Syst., AES-7*, pp. 499–505.

Raney, R. K., and R. A. Shuchman, 1978. SAR Mechanism for Imaging Waves, *Proc. Fifth Canadian Symp. on Remote Sensing*, Victoria, B. C.

Shemdin, O. H., 1980. The Marineland Experiment: An Overview, *Trans. Amer. Geophys. Union, 61*, No. 38, pp. 625–626.

Shuchman, R. A., 1981. Processing Synthetic Aperture Radar Data of Ocean Waves, *Oceanography from Space*, ed. by J. F. R. Gower, Plenum Press, New York, pp. 477–496.

———, 1982. *Quantification of SAR Signatures of Shallow Water Ocean Topography*, Univ. of Mich. PhD Dissertation, Ann Arbor, MI, 130 p.

Shuchman, R. A., and E. S. Kasischke, 1979. The Detection of Oceanic Bottom Topographic Features Using SEASAT Synthetic Aperture Radar Imagery, *Proc. Thirteenth Int. Symp. Remote Sens. Environ.*, pp. 1277–1292.

———, 1981. Refraction of Coastal Ocean Waves, in *Spaceborne Synthetic Aperture Radar for Oceanography*, ed. by R. C. Beal, P. S. DeLeonibus, and I. Katz, Johns Hopkins Univ. Press, Baltimore, MD, pp. 128–135.

Shuchman, R. A., C. L. Rufenach, F. I. Gonzalez, and A. Klooster, 1979. The Feasibility of Measurement of Ocean Surface Currents Using Synthetic Aperture Radar, *Proc. Thirteenth Int. Symp. Remote Sens. Environment*, Ann Arbor, MI, pp. 93–102.

Shuchman, R. A., A. L. Maffett, and A. Klooster, 1981. Static Modeling of a SAR Imaged Ocean Scene, *IEEE J. Oceanic Eng., OE-6*, pp. 41–49.

Thorpe, S. A., 1975. The Excitation, Dissipation, and Interaction of Internal Waves in the Deep Ocean, *J. Geophys. Res., 80*, pp. 328–338.

Vesecky, J. F., and R. H. Stewart, 1982. The Observation of Ocean Surface Phenomena Using Imagery from the Seasat Synthetic Aperture Radar—An Assessment, *J. Geophys. Res., 87*, pp. 3397–3430.

Vesecky, J. F., H. M. Assal, R. H. Stewart, R. A. Shuchman, E. S. Kasischke, and J. D. Lyden, 1982. Seasat-SAR Observations of Surface Waves, Large Scale Surface Features and Ships During the JASIN Experiment, *1982 Int. Geoscience and Remote Sensing Symposium Digest*, pp. WP-1, 1.1–1.6.

Wright, J. W., 1966. Backscattering from Capillary Waves with Application to Sea Clutter, *IEEE Trans. Antenna Propagat., AP-14*, pp. 749–754.

Wunch, C., 1976. Geographical Variability of the Internal Wave Field: A Search for Sources and Sinks, *J. Phys. Ocean., 6*, pp. 471–485.

Zwamborn, J. A., 1979. Analysis of Causes of Damage to Sines Breakwater, *Coastal Structures 79, Vol. 8*, American Society of Civil Engineers, New York, NY, pp. 422–441.

(Received 5 September 1982; revised and accepted 13 March 1983)

Eighteenth International Symposium on Remote Sensing of Environment

Paris, France
1-5 October 1984

Organized and conducted jointly by the Centre National d'Etudes Spatiales (CNES) and the Environmental Research Institute of Michigan (ERIM), the Symposium will address state-or-the-art capabilities and techniques, emphasizing current and future capabilities for remote sensing from space.

The technical program will include conventional presentations and multidisciplinary poster sessions formulated to address

- Current techniques and operational applications, emphasizing land and ocean monitoring, including Earth resources and environmental surveys, inaccessible regions, disaster assessment, vegetation mapping, and cartographic applications.
- Advanced techniques and methodology, including statistical methods, inventory strategies, simulation methods, multiple sensors and observations, angular variations, topographic effects, data handling, processing, and analysis.
- Socio-economic considerations, including economic impact, training and technology transfer, commercial operation, and the role of industry.
- Future Earth observation from space. Advanced sensors and sensor systems; data collection, transmission, reception, and dissemination; and data processing and analysis techniques.

For more information please contact

Alain Gaubert
CNES
42, rue Cambronne
75015 Paris, France
Tele. 1.306.26.40

Jerald J. Cook
ERIM
P. O. Box 8618
Ann Arbor, MI 48107
Tele. (313) 994-1200